Nanoscale

Accepted Manuscript

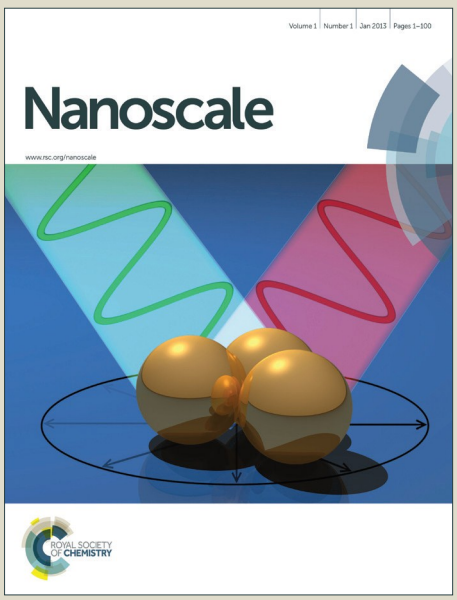

ROYAL SOCIETY OF CHEMISTRY

www.rsc.org/nanoscale

Journal Name

COMMUNICATION

Facile Fabrication of $BiVO_4$ Nanofilms with Controlled Pore Size and their Photoelectrochemical Performances

Received 00th January 20xx,
Accepted 00th January 20xx

DOI: 10.1039/x0xx00000x

www.rsc.org/

Chenchen Feng[a], Zhengbo Jiao[a], Shaopeng Li[a], Yan Zhang[b], and Yingpu Bi[a,*]

We demonstrate a facile method for the rational fabrication of pore-size controlled nanoporous $BiVO_4$ photoanodes, and confirmed that the optimum pore-size distributions could effectively absorb the visible light through the light diffraction and confinement functions. Furthermore, *in-situ* X-ray photoelectron spectroscope (XPS) reveals the more efficient photoexcited electron-hole separation than conventional particle films, induced by light confinement and rapid charge transfer in the inter-crossed worm-like structures.

Photoelectrochemical (PEC) water splitting is a promising approach for solving current energy and environment crisis, by which the abundant solar energy could be converted into chemical fuels.[1-3] However, the construction of the high performance PEC devices toward practical applications generally requires highly efficient and stable photocathodes and photoanodes for both hydrogen and oxygen evolving reactions.[4,5] In contrast to the significant development of the photocathodes, the efficiency of photoanodes for water oxidation is presently limited due to the high overpotential (>0.35 V) as well as complex proton-coupled electron transfer reactions.[6] Generally, metal oxides are promising photoanode materials due to their low-cost synthetic routes and higher stability than other semiconductors.[7] However, most materials studied to date suffer from inadequate band structures (band gap, conduction and valence band energy levels, charge carrier mobilities, etc.) For instance, the commonly binary oxides TiO_2 and ZnO have band gaps that are too large to absorb light efficiently (3.2 and 3.4 eV, respectively), while the Fe_2O_3, despite its desirable band gap of ~2.2 eV, has a conduction band edge at 0.55 V versus the reversible hydrogen electrode (RHE), which exhibit poor charge transport properties as well as low charge separation.[8-10] Thereby, it is highly desirable for the exploring and fabricating novel semiconductor materials with appropriate band-gap for improving the PEC performances.

With a band gap of 2.4 eV (520 nm) and high conduction band energy relative to other visibly active metal oxides, bismuth vanadate ($BiVO_4$) has become an especially promising photoanode material for water oxidation.[11-16] However, its practical applications for water oxidation are still hindered due to higher electron-hole recombination rates and low charge transport properties.[17-20] Thus, various attempts have been implemented to improve the performances of $BiVO_4$-based photoanodes, such as varying film thickness,[18,21,22] metal ions doping,[23-27] and co-catalyst deposition,[17,28-30] and some important developments have been achieved. More recently, mesoporous $BiVO_4$ photoanodes with large surface areas have received increasing attention owning to their higher photoelectrochemical properties compared with the compact solid counterparts.[31-34] However, the present fabrication methods of nanoporous $BiVO_4$ photoanodes were generally based on the template-assisted replacement methods, and their pore-size distributions cannot be rationally tailored.

Herein, we demonstrate a general and template-less method for one-step construction of pore-size controllable $BiVO_4$ nanoporous films. Benefiting from unique structural features, the as-prepared $BiVO_4$ with pore size distribution of 300-400 nm could show enhanced light adsorption, charge separation and photo-electrochemical properties. Importantly, the origin of high efficient photoelectric conversion in nanoporous $BiVO_4$ photoanodes have been explored and clarified. More specifically, the visualized evidence for more efficient electron-hole separation in nanoporous $BiVO_4$ film than traditional particle films has been achieved by using a powerful *in-situ* XPS technique. Moreover, the optical tests confirmed the evident light confinement effect in nanoporous structures for effectively trapping visible-light.

The nanoporous $BiVO_4$ films grown on FTO substrate were fabricated through a simple coating and thermal treatment method, and a schematic illustration on the synthetic procedure was shown in Figure S1 (Supporting Information). Figure 1 shows the typical scanning electron microscope (SEM) images of as-prepared $BiVO_4$ samples. It can be seen from Figure 1A that the nanoporous

[a] *State Key Laboratory for Oxo Synthesis & Selective Oxidation, National Engineering Research Center for Fine Petrochemical Intermediates Lanzhou Institute of Chemical Physics, CAS, Lanzhou, Gansu 730000 (P.R. China)*
E-mail: yingpubi@licp.cas.cn
[b] *College of Physics and Electronic Engineering, Northwest Normal University, Lanzhou 730070 (P.R. China)*
† Electronic Supplementary Information (ESI) available. See DOI: 10.1039/x0xx00000x

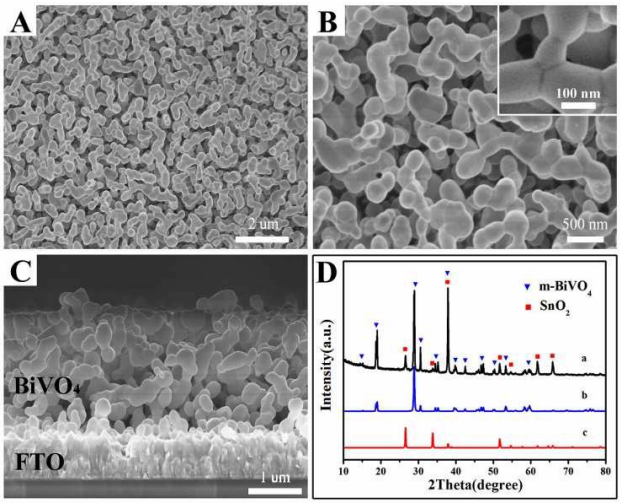

Figure 1. Top (A), (B) and side view (C) SEM images of $BiVO_4$-c; (D) XRD of $BiVO_4$-c. (b) Standard XRD pattern of $BiVO_4$ (JCPDS, No. 14-688), (c) standard XRD pattern of SnO_2 (JCPDS, No. 77-450).

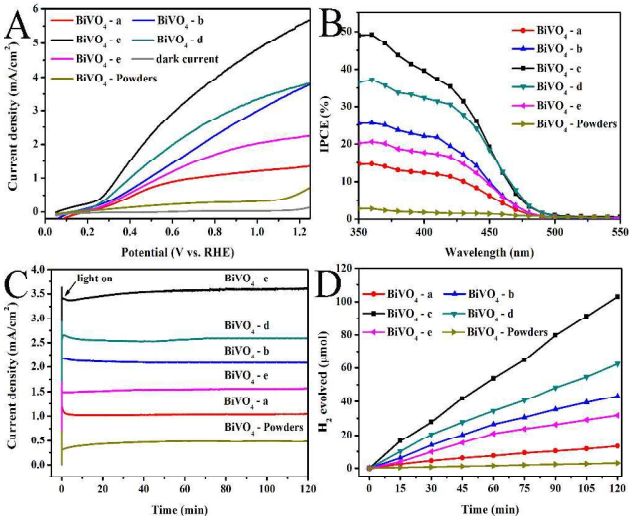

Figure 2. (A) Current-Potential characteristics, (B) the incident photon-to-current conversion efficiency (IPCE), (C) i-t curve and (D) the production of H_2. All performances were measured at 0.7 V (vs. RHE) in a 0.5 M phosphate buffers (pH 7) containing 1 M Na_2SO_3, with a 420 nm cut-off filter, 200 mW/cm^2 illumination.

structure is composed of tightly connected wormlike structures with amounts of void spaces in the range of 300-400 nm (Figure S2C, Supporting Information). More specifically, the enlarged SEM image (Figure 1B) clearly reveals that this wormlike structure is constructed by numerous inter-crossed nanoparticles with the main diameters of 200-300 nm (inset of Figure 1B). The cross-section SEM images of the porous films are also presented in Figure 1C, and obvious pores throughout the entire films can be observed. Furthermore, their crystalline structure as well as compositions has been measured by the X-ray diffraction (XRD). As can be seen from Figure 1D, except for the diffraction peaks of SnO_2 from FTO substrate, all the characteristic peaks could be indexed to the monoclinic bismuth vanadate (JCPDS, No. 14-688). Moreover, the trans-mission electron microscopy (TEM) and selective area electron diffraction (SAED) images (Figure S3, Supporting Information) clearly reveal that these porous structures are composed of the irregular inter-crossed nanoparticles with single crystalline structure. The EDS as well as mapping images confirm the Bi, V, and O elements in the whole area. For comparison, SEM images of nanoparticle $BiVO_4$ powders films have been shown in Figure S4 (Supporting Information). It is clearly to see that a compact powders films were consisted of disorganized nanoparticles.

Furthermore, the pore diameters of the $BiVO_4$ films could be rationally tailored by simply adjusting the ratios of PEG-600 in the precursor solution, and the corresponding SEM images were showed in Figure S5 (Supporting Information). With the decreasing PEG-600 concentrations, the void spaces as well as pore diameters of the $BiVO_4$ films gradually decreased (Figure S5A and S5B). In contrast, the void spaces as well as pore diameters in final $BiVO_4$ films could be further enlarged. XRD measurements of other $BiVO_4$ films with different amounts of PEG-600 were also performed (Figure S6, Supporting Information). It is obvious that the XRD patterns of all samples are exactly similar, in other words, the existence of PEG-600 completely does not influence the crystal structure of $BiVO_4$ films. Therefore, it can be concluded that in the present fabrication system, the PEG-600 serves as a decisive role for adjusting the pore diameters, and the formation of nanoporous structure should be due to the carbonification of PEG-600 during anneal process in air at 500 °C.

The photoelectrochemical properties of as-synthesized nanoporous $BiVO_4$ samples with different pore sizes (marked from $BiVO_4$-a to $BiVO_4$-e) were explored in the presence of 1 M sodium sulfite (Na_2SO_3) under visible-light irradiation ($\lambda > 420$nm). For comparison, the related performances of conventional $BiVO_4$ particle films have also been studied and compared in Figure 2. It can be clearly seen that except for particle films, all the nanoporous $BiVO_4$ photoelectrodes exhibit high photocurrent-potential (J-V) curves for the sulfite oxidation (Figure 2A). Furthermore, a very low photocurrent onset potential, 0.1 V versus reversible hydrogen electrode (RHE), this value corresponds to the flatband potential (Figure S7, Supporting Information), and a rapid increase in photocurrent from 0.2 V versus RHE, demonstrating the excellent fill factor and electron-hole separation under visible-light irradiation. More specifically, the nanoporous $BiVO_4$-c sample (shown in Figure 1) exhibits the highest photocurrent density (3.5 mA cm^{-2}) at a potential of 0.7 V vs. RHE for the sulfite oxidation. However, whether increasing or decreasing the pore-diameters of $BiVO_4$ photoelectrodes, the photoelectrochemical properties (shown in Figure S5) have been obviously decreased. On the basis of the above results, it can be concluded that tailoring the pore-diameters could serve as feasible route to further optimize their photoelectric property. In addition, the sulfite oxidation kinetics at the interface of the photoanode/electrolyte was evaluated by electrochemical impedance spectroscopy (EIS), which were presented as Nyquist plots (Figure S8, Supporting Information). The arcs in the Nyquist plot are related to charge transfer at the interface of the electrode/electrolyte. The semicircle arc for the $BiVO_4$-c was lower than that for the $BiVO_4$ particle films, indicating faster sulfite oxidation kinetics. Based on the above results, it can be revealed

that an appropriate pore diameter is beneficial to efficient charge separation and migration.

The further measurements about the incident photon-to-current conversion efficiency (IPCE) of all the $BiVO_4$ nanoporous films and $BiVO_4$ nanoparticles powders have been performed and exhibited in Figure 3B. IPCE analysis of the $BiVO_4$ samples shows a similar distribution compared with Current-Potential characteristics, $BiVO_4$-c reach a maximum of 49% at 350 nm, while the $BiVO_4$ nanoparticles powders achieves 3.7% at this wavelength. The IPCE analysis also shows that the photocurrent response begins at 500 nm, this corresponds to the band gap of 2.47 eV for $BiVO_4$ (Figure S9, Supporting Information). Then, the photocurrent density of samples was maintained for 120 min by applying 0.7 V (vs. RHE) without showing wide decay or rise, proving its long-term stability (Figure. 4C). Figure 4D shows hydrogen evolution versus time at the Pt counter electrode for the $BiVO_4$ nanoporous films and particle films, H_2 generation was detected with Gas Chromatography (GC). It was found solar light irradiation and applying bias voltage (0.7 V vs. RHE) resulted in continuous H_2 evolution from an electrolyte by $BiVO_4$ photoelectrodes. Besides, during the H_2 production procedure, the amount of H_2 is linearly related to the reaction time. Finally, the maximum amount of the H_2 generated by the $BiVO_4$-c was 102.8 μmol after 120 min. On the contrary, the $BiVO_4$ nanoparticles powders only produce trace amounts of H_2 (3.1 μmol after 120 min) under the same conditions, indicating the poor reduction power of photogenerated electrons in nanoparticles $BiVO_4$ powders when comparing with that of nanoporous $BiVO_4$ photoelectrodes. While the water oxidation is much more difficult than Na_2SO_3 oxidation, and Na_2SO_3 was employed as the hole scavenger for the PEC tests in this work. To further illustrate the characteristic photo-electrochemical properties of nanoporous $BiVO_4$ photoelectrodes, $BiVO_4$ electrodes were loaded with Co-Pi cocatalyst by the in situ photochemical deposition method.[36] The typical current-potential curves of water oxidation and hydrogen evolution are shown in Figure S10 (Supporting Information). It can be clearly seen that the $BiVO_4$ nanofilms with pore size distribution of 300-400 nm still exhibited the highest photoelectrochemical properties as well as hydrogen generation rates despite of the variations of electrolyte and light irradiations.

A novel in-situ X-ray photoelectron spectroscopy (XPS) combined with synchronous illumination technique was firstly employed for the direct observation of charge generation and transfer direction in nanoporous $BiVO_4$ sample (Figure S11). As we can see in Figure 3, before the irradiation, two strong peaks in the Figure 3A, at 164.28 eV and 158.9 eV, are indexed to Bi 4f5/2 and Bi 4f7/2, demonstrating the Bi^{3+} species in the $BiVO_4$ samples. Amazingly, when the sample was irradiated by visible-light, the bind energies of both Bi 4f5/2 and Bi 4f7/2 peaks obviously shifted to the low values, while these two peaks returned to the original positions when light was turned off. Simultaneously, the similar photoinduced shift on the V 2p1/2 and V 2p3/2 peaks could also be observed (Figure 3B). As for the O 1s $BiVO_4$ nanoporous films, apart from the peak of lattice oxygen at 529.5 eV, an additional peak at 532.2 eV can be attributed to hydroxyls binding.[24,35] The peak of hydroxyls binding continuously shifts to left (BE become higher) when light on, but the peak of lattice oxygen first shifts to left when light on and return to original position (Figure 3C). Thereby, it can

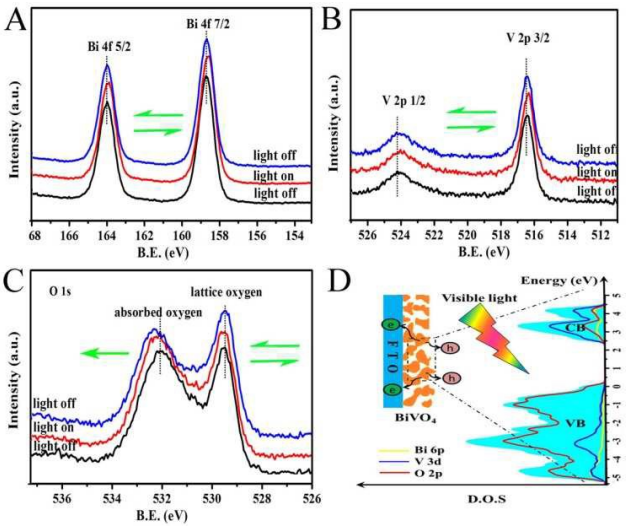

Figure 3. (A-C) In situ Bi 4f, V 2p, O 1s XPS spectra of $BiVO_4$-c films, and all the samples were irradiated by visible light. (D) Calculated total and partial density of states for $BiVO_4$, the top of the valence band is shifted to zero.

be concluded that such a photoinduced shift for nanoporous $BiVO_4$ film may be attributed to trapping of photogenerated electrons by Bi, V sites and holes by O site during the visible-light irradiation, and this process is reversible for Bi, V sites and lattice oxygen. However, in the case of traditional $BiVO_4$ particle films, no evident shift of all peaks could be observed whether under light or in dark (Figure S12, Supporting Information). As shown in Figure 3D, the valence band of $BiVO_4$ is mainly composed of O 2p, and the conduction band is formed by V 3d, O 2p, and Bi 6p. The photoexcited electrons are mostly transferred from O to V and Bi, which is consistent with the above *in-situ* XPS results. More specifically, these demonstrations clearly reveal more efficient charge separation and transfer in the nanoporous structure than compact particles, which resulted in the enhancement in PEC activity.

The reflection, transmission and absorption spectra of in both nanoporous and compact structures have been studied and shown in Figure 4. It can be seen that the absorption edge of both the porous and the compact film is at about 520 nm, corresponding to a band gap of 2.4 eV. However, compared to particle films, nanoporous structure could effectively enhance light harvesting in both ultraviolet and visible light regions. Moreover, the porous structure possesses higher transmission and lower reflection than compact $BiVO_4$ films. In addition, the light transmission in both nanoporous and particle structures has been studied by using different mono-chromatic lights. Obviously, all the monochromatic lights could permeate the porous films and no evident changes about light facula have been observed. In contrast, evident light-scattering phenomena have been observed, especially in the monochromatic lights with large wavelength. Besides, we measured the light intensity of the monochromatic light transmission before and after (Table S2, Supporting Information). The weakening extent of the light intensity for $BiVO_4$ nanoporous photoanodes is far below powders photoanodes. Herein, we consider that some possible reasons are responsible for above optical phenomena and the schematic illustration has been shown in Figure 5. Optical

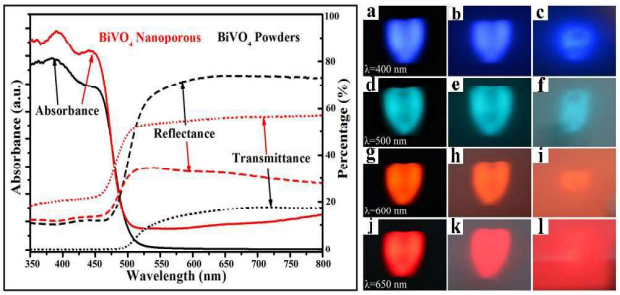

Figure 4. Absorption, transmission and reflection spectra of $BiVO_4$ nanoporous and powders photoanodes. The transmission phenomena of $BiVO_4$ nanoporous (b, e, h, k) and powders (c, f, i, l) photoanodes in the monochromatic lights with different wavelengths.

system diagram of the monochromatic light transmission has been shown in Figure S13 (Supporting Information). One is stronger multiple light diffraction in a porous sample, and the other is light confinement effect. The porous film is recognized to enhance the light harvesting due to light diffraction within the pores by increasing the optical path length of light, especially in the wavelength range corresponding to the band edge. However, the stronger light-scattering and reflection in compact films resulted in the lower light absorption phenomena. These demonstrations clearly reveal the multiple light diffraction and confinement effect in a nanoporous structure and provide a new strategy to designing a higher efficiency device for solar conversion and storage. On the other hand, $BiVO_4$ nanoporous and powders photoanodes show apparent hydrophilic differences (Figure S14), and their contactangle are 10.4° and 30.1°, respectively. Excellent hydrophilicity of $BiVO_4$ nanoporous photoanodes could facilitate electrolyte to immerse into films contributing to the enhanced surface reaction kinetics and carrier separation, which should be another important reason for the remarkable photoelectrochemical properties of $BiVO_4$ nanoporous photoanodes.

In addition, the time-resolved photoluminescence (PL) spectra (Figure S15 and Table S3) have been measured to reveal the recombination and lifetime of photoinduced charge. As shown in Figure S15A, the nanoporous $BiVO_4$ possess more efficient charge separation and longer lifetime than traditional $BiVO_4$ powders, which should be attributed to the light confinement and charge Transfer as a result of porous structure. Furthermore, the trend of PL lifetime change of $BiVO_4$ nanoporous with controllable pore size (Figure S15B) is consistent with their PEC properties variation. These demostrations clearly reveal that tailoring the pore sizes (i.e.

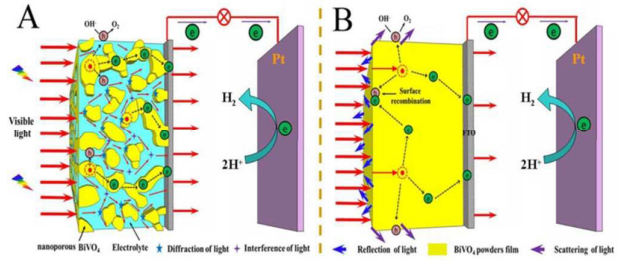

Figure 5. Schematic illustration of the transport process of photogenerated carriers and spread path of the light for $BiVO_4$ nanoporous (A) and powders (B) photoanodes.

300-400 nm) of $BiVO_4$ nanoporous photoanodes could effectively optimize the charge eparation and transfer for enahcning catalytic properties.

In summary, we have developed a simple coating combined with heat treatment strategy for fabricating pore-diameter controlled $BiVO_4$ photoanodes. Furthermore, it has been found that these nanoporous $BiVO_4$ photoanodes with an appropriate pore-diameter (300-400 nm) exhibited the remarkable photoelectro-chemical performance under visible light radiation. More importantly, it has been firstly reported that the multiple light diffractions of nanoporous structures play a crucial role in determining the higher photo-electrochemical properties. Moreover, the nanoporous structure could facilitate the high charge separation efficiency and rapid hole transfer as a result of the facile infiltration of electrolyte into nanoporous films. Finally, these demonstrations can deepen understanding on light confinement and charge transfer states and provide a new strategy to optimize other semiconductor photoanodes.

Acknowledgements

This work was supported by the "Hundred Talents Program" of the Chinese Academy of Science and the National Natural Science Foundation of China (21573264, 21273255, 21303232).

Notes and references

1 K. Oscar, and J. A. Turner, *Science*. 1998, **280**, 425.
2 T. Hisatomi, J. Kubota and K. Domen, *Chem. Soc. Rev*. 2014, **43**, 7520.
3 M. G. Walter, E. L. Warren, J. R. McKone, S. W. Boettcher, Q. Mi, E. A. Santori and N. S. Lewis, *Chem. Rev*. 2010, **110**, 6446.
4 F. E. Osterloh, *Chem. Soc. Rev*. 2013, **42**, 2294.
5 J. Zhang, W. Zhao, Y. Xu, H. Xu and B. Zhang, *Int. J. Hydrogen Energy*, 2014, **39**, 702.
6 F. M. Toma, A. Sartorel, M. Iurlo, M. Carraro, P. Parisse, C. Maccato, S. Rapino, B. R. Gonzalez, H. Amenitsch, T. D. Ros, L. Casalis, A. Goldoni, M. Marcaccio, G. Scorrano, G. Scoles, F. Paolucci, M. Prato and M. Bonchio, *Nature Chemistry*. 2010, **2**, 826.
7 B. D. Alexander, P. J. Kulesza, I. Rutkowska, R. Solarska and J. Augustynski, *J. Mater. Chem*, 2008, **18**, 2298.
8 H. Irie, Y. Watanabe and K. Hashimoto, *J. Phys. Chem. B*, 2003. **107**, 5483.
9 Ü. Özgür, Y. I. Alivov, C. Liu, A. Teke, M. Reshchikov, S. Doğan and H. Morkoc, *J. Appl. Phys*, 2005, **98**, 041301.
10 D. K. Zhong, J. Sun, H. Inumaru and D. R. Gamelin, *J. Am. Chem. Soc*, 2009, **131**, 6086.
11 A. Walsh, Y. Yan, M. N. Huda, M. M. Al-Jassim and S. H. Wei, *Chem. Mater*, 2009, **21**, 547.
12 W. J. Yin, S. H. Wei, M. M. Al-Jassim, J. Turner and Y. Yan, *Phys. Rev. B*. 2011, **83**, 155102.
13 S. P. Berglund, D. W. Flaherty, N. T. Hahn, A. J. Bard, C. B. Mullins, *J. Phys. Chem. C*. 2011, **115**, 3794.
14 A. Kudo, K. Ueda, H. Kato and I. Mikami, *Catal. Lett*, 1998, **53**, 229.
15 A. Iwase and A. Kudo, *J. Mater. Chem*, 2010, **20**, 7536.
16 X. Shi, Y. Choi, K. Zhang, J. Kwon, D. Y. Kim, J. K. Lee, S. Ho Oh, J. K. Kim and J. H. Park, *Nat. Commun.*, 2014. **5**, 4775.
17 D. K. Zhong, S. Choi and D. R. Gamelin, *J. Am. Chem. Soc*, 2011, **133**, 18370.

18 F. F. Abdi and R. vande Krol, *J. Phys. Chem. C*, 2012, **116**, 9398.
19 A. J. E. Rettie, H. C. Lee, L. G. Marshall, J. F. Lin, C. Capan, J. Lindemuth, J. S. McCloy, J. Zhou, A. J. Bard and C. B. Mullins, *J. Am. Chem. Soc*, 2013, **135**, 11389.
20 F. F. Abdi, T. J. Savenije, M. M. May, B. Dam and R. van de Krol, *J. Phys. Chem. Lett*, 2013, **4**, 2752.
21 Y. Liang, T. Tsubota, L. P. Mooij and R. van de Krol, *J. Phys. Chem. C*, 2011, **115**, 17594.
22 F. F. Abdi and R. van de Krol, *J. Phys. Chem. C*, 2012, **116**, 9398.
23 H. S. Park, K. E. Kweon, H. Ye, E. Paek, G. S. Hwang and A. J. Bard, *J. Phys. Chem. C*, 2011, **115**, 17870.
24 S. P. Berglund, A. J. E. Rettie, S. Hoang and C. B. Mullins, *Phys. Chem. Chem. Phys*, 2012, **14**, 7065.
25 K. P. Parmar, H. J. Kang, A. Bist, P. Dua, J. S. Jang and J. S. Lee, *ChemSusChem*, 2012, **5**, 1926.
26 F. F. Abdi, N. Firet and R. van de Krol, *ChemCatChem*, 2013, **5**, 490.
27 K. Zhang, X. Shi, J. K. Kim and J. H. Park, *Phys. Chem. Chem. Phys*, 2012, **14**, 11119.
28 J. A. Seabold and K. -S. Choi, *J. Am. Chem. Soc*, 2012, **134**, 2186.
29 S. K. Pilli, T. E. Furtak, L. D. Brown, T. G. Deutsch, J. A. Turner and A. M. Herring, *Energy Environ. Sci*, 2011, **4**, 5028.
30 T. W, Kim and K. S. Choi, *Science*, 2014, **343**, 990.
31 K. J. McDonald and K. S. Choi, *Energy Environ. Sci*, 2012, **5**, 8553.
32 X. Zhao, W. J. Luo, J. Y. Feng, M. X. Li , Z. S. Li, T. Yu and Z. G. Zou, *Adv. Energy Mater*, 2014, **4**, 1301785.
33 M. Ma, J. K. Kim, K. Zhang, X. Shi, S. J. Kim, J. H. Moon and J.H. Park, *Chem. Mater*. 2014, **26**, 5592.
34 Z. Chen, T. F. Jaramilloa1, T. G. Deutscha, A. Kleiman-Shwarscteina, A. J. Formana, N. Gaillarda, R. Garlanda, K. Takanabea, C. Heskea, M. Sunkaraa, E. W. McFarlanda, K. Domena, E. L. Millera, J. A. Turner and H. N. Dinha, *J. Mater. Res*, 2010, **25**, 3.
35 H. Bluhm and J. Electron Spectrosc, *Relat. Phenom*, 2010, **177**, 71.
36 D. Wang, R. Li, J. Zhu, J. Shi, J. Han, X. Zong and C. Li, *J. Phys. Chem. C*, 2012, **116**, 5082.